

Resonant plasmonic terahertz detection in gated graphene p-i-n field-effect structures enabled by the Zener-Klein tunneling nonlinearity

V. Ryzhii¹, T. Otsuji¹, M. Ryzhii², V. Mitin³, and M. S. Shur⁴

¹Research Institute of Electrical Communication, Tohoku University, Sendai 980-8577, Japan

²Department of Computer Science and Engineering,
University of Aizu, Aizu-Wakamatsu 965-8580, Japan

³Department of Electrical Engineering, University at Buffalo, SUNY, Buffalo, New York 14260 USA

⁴Department of Electrical, Computer, and Systems Engineering,
Rensselaer Polytechnic Institute, Troy, New York 12180, USA

We propose and analyze the terahertz (THz) detectors based on a gated graphene p-i-n (GPIN) field-effect transistor (FET) structure. The reverse-biased i-region between the gates plays the role of the electrons and holes injectors exhibiting nonlinear $I - V$ characteristics due to the Zener-Klein tunneling. This region enables the THz signal rectification, which provides their detection. The gated regions serve as the electron and hole reservoirs and the THz resonant plasma cavities. The resonant excitation of the electron and hole plasmonic oscillations results in a substantial increase in the THz detector responsivity at the signal frequency close to the plasma frequency and its harmonics. Due to the specifics of the i-region AC conductance frequency dependence, associated with the transit-time effects, the GPIN-FET response at the frequency, corresponding to the excitation of a higher plasmonic mode, can be stronger than for the fundamental mode. The GPIN-FETs can exhibit fairly high responsivity at room temperatures. Lowering of the latter can result in its further enhancement due to weakening of the carrier momentum relaxation.

I. INTRODUCTION

Field-effect transistors (FETs) using plasmonic effects can serve as effective terahertz (THz) radiation detectors [1]. The FET THz detectors with the graphene channel can exhibit markedly enhanced performance [2, 3] due to the unique electron (hole) transport properties of graphene, in particular, high electron mobility and directed velocity at elevated temperatures. Different mechanisms enable the THz signals rectification in plasmonic FET detectors, for example, the hydrodynamic nonlinearity mechanism, the barrier rectification in the Schottky junctions, p-n-junctions, or electrostatic barriers, and others (see, for example [4–13]). The specific features of the graphene band structure enable the Zener-Klein interband tunneling [14–19]. The Zener-Klein tunneling leads to nonlinear $I - V$ characteristics of different graphene devices. This nonlinearity can be used for the rectification of the THz signals and their detection. In this paper, we evaluate the proposed THz detector based on a lateral graphene p-i-n FET (GPIN-FET) detector structure with the gated p- and n-regions of the graphene layer (GL) channel. The detection of the THz signals in this device is associated with the nonlinearity of the i-region $I - V$ characteristics. The plasmonic properties of the gated p- and n-regions enable the resonant response of the GPIN-FETs and lead to their enhanced resonant detector responsivity.

II. MODEL

We consider the GPIN-FET detector structure based on a GL channel embedded in the dielectric (for example, hBN). The channel is covered by two highly conducting gates. The gate voltages of different polarity, $\pm V_g$, are applied to these gates. As a result, the channel comprises the undoped i-regions between the gates (of the length $2l$) and the electrically doped p- and n-regions beneath the gates (of the length L). The lengths of the p- and n-regions are close to the length of the gates (L is somewhat

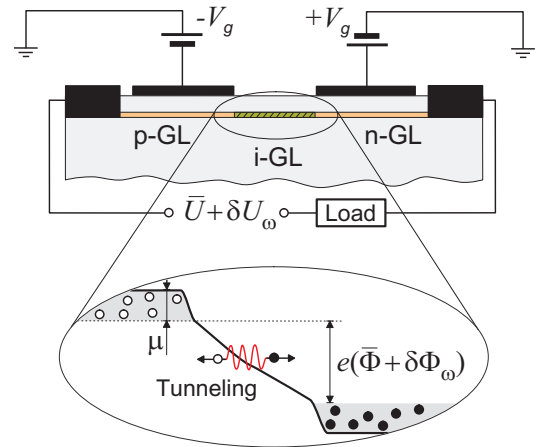


FIG. 1. Schematic view of the cross-sections of the GPIN-FET structure cross-section with gated electrostatically doped p- and n-GLs. Inset shows the potential profile in the GPIN-FET channel.

larger than the gate length due to the finite screening length or the gate fringe effect). The channel is bounded by the source and drain contacts, between which the bias voltage \bar{U} is applied. Figure 1 shows the GPIN-FET structure with the electrically disconnected gates and the potential profile in the GPIN-FET channel at the DC condition (inset) when the bias voltage is applied between the side (source/drain) contacts.

In the present paper, we consider the GPIN-FET structures, where the Coulomb drag effect in the gated regions [20–25] is weak. This corresponds to GPIN-FET structures, in which more liberal and rather practical conditions are fulfilled: stronger scattering on impurities, defects, and acoustic phonons (with the collision frequencies $\nu \gtrsim 1 \text{ ps}^{-1}$), and relatively long gated regions ($L \gtrsim 1 \text{ }\mu\text{m}$). The i-region is assumed to be fairly short [$2l = (0.1 - 0.2) \text{ }\mu\text{m}$], so that the transport of the holes and electrons generated in this region due the Zener-Klein tunneling is ballistic [26–29]. Considering that the i-region is depleted under the operational conditions, the conditions of the ballistic transport in this region with the above length can be realized even at room temperature [30, 31] and, naturally, at lowered temperatures [32]. The holes and electrons generated due to tunneling are directed primarily along the electric field in the i-region, i.e., in the x -direction (the in-plane direction along the GL channel) from the p- and n-region, and propagate ballistically with the velocities, $v = \pm v_W$.

Apart from the DC bias voltage \bar{U} , an AC signal voltage $\delta U_\omega \exp(-i\omega t)$ is applied, where δU_ω and ω are the amplitude and frequency of the incoming THz signal. Thus, the DC and AC voltage drops across the GPIN-FET structure are equal to $\bar{V} = \bar{U} - \bar{U}^{load}$ and $\delta V_\omega = \delta U_\omega - \delta U_\omega^{load}$, where \bar{U}^{load} and δU_ω^{load} are the DC and AC components of the load voltage. These components depend on the load impedance Z^{load} . The latter can be presented as $Z^{load} = [1/r^{load} - i\omega C^{load}]^{-1}$, where r^{load} and C^{load} are the load resistance and capacitance, respectively. We assume that C^{load} is sufficiently large, so that the AC voltage drop across it is negligibly small, therefore, $\delta U_\omega^{load} \simeq 0$ and $\delta V_\omega = \delta U_\omega$. The real part of the load impedance, i.e., its resistance, r^{load} determines the DC output signal.

III. LINEAR RESPONSE

When both the DC voltage \bar{V} and the periodic signal voltage $\delta V_\omega \exp(-i\omega t)$ drop across the GPIN-FET intrinsic part [$V = \bar{V} + \delta V_\omega \exp(-i\omega t)$], the carrier current density in the i-region (and in other sections of the channel) is equal $J^i = \bar{J}^i + \Delta J^i$. Here \bar{J}^i is the DC component. The component ΔJ^i comprises the linear AC component δJ_ω^i proportional to δV_ω and the DC rectified component ΔJ_ω^i . The latter is due to the nonlinear $I - V$ characteristics of the i-region at the conditions of the Zener-Klein tunneling.

The voltage across the devices is distributed between the i-region and the gated regions.

AC conductance of the i-region

Considering the blade-like configuration of the conducting areas surrounding the i-region, the pertinent spatial electric-field distribution in this region [33–36], and using the general formulas for the Zener-Klein tunneling probability in graphene [14–19], one can arrive at the following expression for the DC current density per unit width in the direction along the gate edges [19]:

$$\bar{J} = a \frac{ev_W}{\sqrt{2l}} \left(\frac{e\bar{\Phi}}{\hbar v_W} \right)^{3/2}, \quad (1)$$

where a is a numerical parameter. At moderate $\bar{\Phi}$ when the carrier space-charge in the i-regions is weak,

$$a = \frac{\Gamma(1/4)\Gamma(1/2)}{\Gamma(3/4)} \frac{1}{2\pi^{7/2}},$$

where $\Gamma(z)$ is the Gamma function. Equation (1) corresponds to the i-region linear AC conductance (see Appendix A)

$$\sigma_\omega^i = \sigma^i F_\omega - i\omega c^i = \sigma^i (F_\omega - i\omega \tau^i). \quad (2)$$

Here, $\sigma^i = d\bar{J}^i/d\bar{\Phi}$ is the i-region DC differential conductance, $\tau^i = c^i/\sigma^i$ is the i-region recharging time, and c^i is the geometrical capacitance per unit width of the device determined mainly by the dielectric constant κ of the isolating material surrounding the GL, and geometrical parameters (see, for example, [33–36]). If the GL is deeply embedded into the isolating material $c^i \propto \kappa$. In the case of free GL top surface between the gates, $c^i \propto \kappa^{eff} = (\kappa + 1)/2$. A thin passivation layer can also affect c^i .

According to Eq. (1),

$$\sigma^i = b \frac{e^2}{\hbar} \sqrt{\frac{e\bar{\Phi}}{2l\hbar v_W}}, \quad (3)$$

where $b = 3a/2 \simeq 0.0716$. The quantity

$$F_\omega = \mathcal{J}_0(\omega t^i/2) e^{i\omega t^i/2} \quad (4)$$

reflects the signal frequency dependence of the i-region dynamic conductivity determined by the AC current induced by the carriers propagating between the p- and n-regions (and the pertinent gates), particularly, by the finiteness of their transit time $t^i = 2l/v_W$, where $\mathcal{J}_0(s)$ is the Bessel function of the first kind.

Using Eqs. (2) and (4), we obtain the following expressions for the real and imaginary parts of σ^i :

$$\text{Re } \sigma^i = \sigma^i \mathcal{J}_0(\omega t^i/2) \cos(\omega t^i/2), \quad (5)$$

$$\text{Im } \sigma^i = \sigma^i [\mathcal{J}_0(\omega t^i/2) \sin(\omega t^i/2) - \omega \tau^i]. \quad (6)$$

The quantity $\text{Re } \sigma^i$ can be both positive and negative. However, at $\omega t^i < \pi$, $\text{Re } \sigma^i > 0$. In the range $\omega t^i \lesssim 4.8$, where $\sin(\omega t^i/2) > 0$, the first term in the right-hand side of Eq. (6) is positive. The latter implies that this term corresponds to the kinetic inductance of the holes and electrons in the i-region. In certain ranges of elevated frequencies, the product $\mathcal{J}_0(\omega t^i/2) \sin(\omega t^i/2)$ can be positive, although both factors are negative.

For $2l = 0.2 \mu\text{m}$ and $\bar{\Phi} = 100 - 200 \text{ mV}$, Eqs. (1) and (4) yield $\bar{J}^i \simeq 0.34 - 0.95 \text{ A/cm}$ and σ^i in the range from 520 S/m to 733 S/m (from 4.67 ps^{-1} to 6.59 ps^{-1}). In the case of sufficiently short, i-region the ballistic transport takes place even at higher voltages $\bar{\Phi} > \hbar\omega_0/e$ despite the spontaneous emission of optical phonons, and the current density through this region and, hence, the differential conductance can substantially exceed the above estimates.

Considering Eq. (2), we arrive at the following equation for the linear AC current density in the i-region expressed via the AC potential drop $\delta\Phi_\omega = (\delta\varphi_\omega^i|_{x=l} - \delta\varphi_\omega^i|_{x=-l})$ across this region:

$$\delta J_\omega = \sigma_\omega^i \delta\Phi_\omega \quad (7)$$

Plasmonic response of the gated regions

To express $(\delta\varphi_\omega^i|_{x=l} - \delta\varphi_\omega^i|_{x=-l})$ via δV_ω , we find the spatial distributions of the AC potential in the gated region accounting for its nonuniformity associated with the plasmonic effects.

For the densities of the AC current in p- and n-region ($-L-l < x < -l$ and $l < x < l+L$), we have

$$\delta J_\omega^g = -\sigma_\omega^g L \frac{d\delta\varphi_\omega}{dx} \Big|_{x=\pm l}, \quad (8)$$

where $\sigma_\omega^g = \sigma^g [i\nu/(\omega + i\nu)]$ and $\sigma^g = (e^2\mu/\pi\hbar^2\nu L)$ are the p- and n-regions (gated) AC and DC conductances,

respectively, ν is the frequency of hole and electron momentum relaxation on impurities, acoustic phonons, and $\delta\varphi_\omega = \delta\varphi_\omega(x, y)|_{y=0}$ expresses the ac potential spatial distribution along the axis x directed in the GPIN-FET-channel plane ($y = 0$). The frequency dependence given by Eq. (8) accounts for the kinetic inductance of the gated regions.

For the gated sections of the channel [see Fig. 1(a)], we solve the linearized hydrodynamic equations for the hole and electron plasmas in the related p- and n-regions, disregarding the nonuniformity of the DC potential and carrier density distributions, and arrive at the following equation for the spatial distribution of the ac potential $\delta\varphi_\omega$ accounting for the plasmonic response of the gated regions (see [11] and the references therein):

$$\frac{d^2\delta\varphi_\omega}{dx^2} + \frac{\omega(\omega + i\nu)}{s^2} \left(\delta\varphi_\omega \mp \frac{\eta}{2} \delta V_\omega \right) = 0. \quad (9)$$

Here the upper/lower sign is related to the n-region/p-region, $s = \sqrt{4e^2\mu w/\kappa\hbar^2}$ is the plasma velocity, and $\mu = \mu^p = \mu^n$ is the carrier Fermi energy in the gated regions of both types.

The quantity $\eta = C_{cg}/(C_{cg} + C_g)$ characterizes the contact-gate coupling, where $C_{cg} \propto \kappa$ [or $C_{cg} \propto \kappa^{eff} = (\kappa + 1)/2$] and $C_g = (\kappa L/4\pi w)$ being the pertinent capacitances for the blade-like contacts and gates, where w is the gate layer thickness. Normally, $C_{cg} \ll C_g$, hence $\eta \ll 1$.

Equation (9) governs the AC potential in the p-region ($-L-l < x < -l$) and in the n-region ($l < x < l+L$). It accounts for both the gate and contact-gate capacitances and the kinetic inductance of the holes and electrons in the gated regions.

The boundary conditions at the edges of the gated regions are:

$$\delta\varphi_\omega|_{\pm(l+L)} = \pm \frac{1}{2} \delta V_\omega, \quad (10)$$

$$\sigma_\omega^i (\delta\varphi_\omega|_{x=l} - \delta\varphi_\omega|_{x=-l}) = \sigma_\omega^g L \frac{d\delta\varphi_\omega}{dx} \Big|_{x=\pm l}. \quad (11)$$

Solving Eq. (9) with the boundary conditions given by Eqs. (9) and (10), we obtain

$$\delta\varphi_\omega = \frac{1}{2} \delta V_\omega \left\{ \eta + (1 - \eta) \cos[\alpha_\omega(x - l - L)] + \frac{\eta + (1 - \eta)[\cos(\alpha_\omega L - \xi_\omega(\alpha_\omega L) \sin(\alpha_\omega L)]}{\sin(\alpha_\omega L) + \xi_\omega(\alpha_\omega L) \cos(\alpha_\omega L)} \sin[\alpha_\omega(x - l - L)] \right\} \quad (12)$$

$$\delta\varphi_\omega = -\frac{1}{2} \delta V_\omega \left\{ \eta + (1 - \eta) \cos[\alpha_\omega(x + l + L)] - \frac{\eta + (1 - \eta)[\cos(\alpha_\omega L) - \xi_\omega(\alpha_\omega L) \sin(\alpha_\omega L)]}{\sin(\alpha_\omega L) + \xi_\omega(\alpha_\omega L) \cos(\alpha_\omega L)} \sin[\alpha_\omega(x + l + L)] \right\} \quad (13)$$

for the n-region and p-region), respectively.

Here $\varkappa_\omega = \pi\sqrt{\omega(\omega+i\nu)}/2\Omega L$, $\xi_\omega = \sigma_\omega^g/2\sigma_\omega^i = (\sigma_\omega^g/2\sigma_\omega^i)[i\nu/(\omega+i\nu)] = (\sigma_\omega^g/2\sigma_\omega^i)[i\nu/(\omega+i\nu)(F_\omega - i\omega\tau^i)]$, and

$$\Omega = \frac{\pi e}{\hbar L} \sqrt{\frac{\mu w}{\kappa}} \quad (14)$$

is the plasma frequency of the gated regions (see for example, [13, 37–40]). Here we assumed that the electron liquid in the gated portion of the channel at the carrier densities under consideration is degenerate.

Considering that $\delta\Phi_\omega = (\delta\varphi_\omega|_{x=l} - \delta\varphi_\omega|_{x=-l})$ and using Eqs. (12) and (13), we obtain

$$\delta\Phi_\omega = P_\omega \delta V_\omega, \quad \delta J_\omega = \sigma_\omega^i P_\omega \delta V_\omega \quad (15)$$

with $\delta V_\omega = \delta U_\omega$. Here

$$P_\omega = \frac{\eta \cos(\varkappa_\omega L) + 1 - \eta}{\cos(\varkappa_\omega L) + \frac{1}{\xi_\omega} \frac{\sin(\varkappa_\omega L)}{(\varkappa_\omega L)}}. \quad (16)$$

Considering that in the real case $\eta \ll 1$, the function P_ω is weakly sensitive to the contact-gate capacitive coupling, in particular, to the parasitic capacitance C_{cg} (see Sec. VII), and Eq. (16) can be somewhat simplified as follows:

$$P_\omega \simeq \frac{1}{\cos(\varkappa_\omega L) + \frac{1}{\xi_\omega} \frac{\sin(\varkappa_\omega L)}{(\varkappa_\omega L)}}. \quad (17)$$

IV. RECTIFIED CURRENT AND PLASMONIC FACTOR

The $I - V$ characteristic given by Eq. (1) corresponds to the nonlinear current density component, which comprises the rectified component and the AC current harmonics:

$$\Delta\tilde{J}_\omega = \beta \delta\Phi_\omega^2, \quad (18)$$

where

$$\beta = \frac{1}{2} \frac{d^2\tilde{J}}{d\Phi^2} = \frac{\sigma^i}{4\Phi} = \frac{be^{5/2}}{4\sqrt{2l\hbar^3 v_W \Phi}} \propto \frac{1}{\sqrt{\Phi}} \quad (19)$$

is the parameter characterizing the nonlinearity of the i-region tunneling $I - V$ characteristics given by Eq. (1), i.e., the curvature of these characteristic.

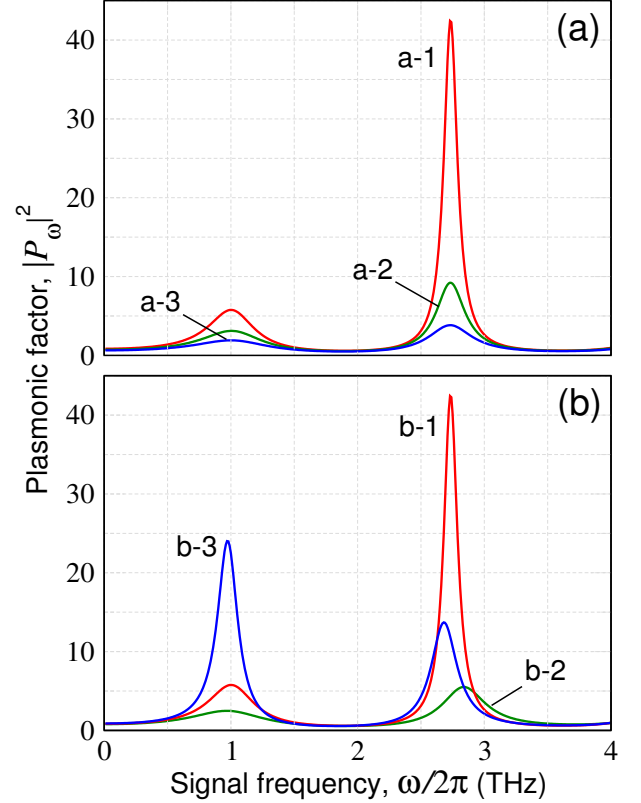


FIG. 2. Plasmonic factor $|P_\omega|^2$ versus signal frequency $f = \omega/2\pi$ (a) for GPIN-FETs (a-1) - (a-3) with different values of frequency, ν , of the carrier momentum relaxation in the gated regions and, consequently, different conductivity, σ^g , of these regions and (b) for GPIN-FETs (b-1) - (b-3) with different lengths of the i-region $2l$, corresponding to different differential conductivity σ^i , and transit time t^i ($\bar{U} = 200$ mV). The parameters of the samples are given in Table I.

According to the Kirchhoff low,

$$\bar{\Phi} = \frac{\bar{U}}{\gamma}, \quad \delta\Phi_\omega = \delta U_\omega, \quad (20)$$

where $\gamma = 1 + 2H\sigma^i r^{load}/3$. Here we accounted for that the i-region DC conductance is equal to $2\sigma^i/3$.

Equation (18) yields the following expression for the density of the rectified current $\Delta\tilde{J}_\omega = (\omega/2\pi) \int_0^{2\pi/\omega} dt \Delta\tilde{J}_\omega$:

$$\Delta\tilde{J}_\omega = \frac{\sigma^i}{8\Phi} |P_\omega|^2 \delta\Phi_\omega^2 = \frac{\sigma^i \gamma}{8U} |P_\omega|^2 \delta U_\omega^2. \quad (21)$$

As seen from Eq. (21), the rectified current density $\Delta\tilde{J}_\omega$, as will be seen in the following, and the frequency dependence of the GPIN-FET detector responsivity, are

TABLE I. GPIN-FET parameters (* samples with identical parameters)

Sample	$2l$ (μm)	t^i (ps)	τ^i (ps)	L (μm)	w (nm)	κ	μ (meV)	ν (ps^{-1})	$\sigma^g/2\sigma^i$	$\Omega/2\pi$ (THz)
a-1*	0.2	0.2	0.1	1.0	15	4.5	100	1.0	12	1.0
a-2	0.2	0.2	0.1	1.0	15	4.5	100	2.0	6	1.0
a-3	0.2	0.2	0.1	1.0	15	4.5	100	3.0	4	1.0
b-1*	0.2	0.2	0.1	1.0	15	4.5	100	1.0	12	1.0
b-2	0.1	0.1	0.1	1.0	15	4.5	100	1.0	8.5	1.0
b-3	0.4	0.4	0.1	1.0	15	4.5	100	1.0	16.9	1.0
c-1*	0.2	0.2	0.1	1.0	15	4.5	100	1.0	12	1.0
c-2	0.2	0.2	0.1	1.0	15	4.5	144	1.0	14.4	1.2
c-3	0.2	0.2	0.1	1.0	15	4.5	64	1.0	9.6	0.8
d-1*	0.2	0.2	0.1	1.0	15	4.5	100	1.0	12	1.0
d-2	0.2	0.2	0.2	1.0	33	10.0	100	1.0	12	1.0
d-3	0.2	0.2	0.3	1.0	50	15.0	100	1.0	12	1.0

determined by the plasmonic factor $|P_\omega|^2$. This factor is given by Eq. (16):

$$|P_\omega|^2 = \left| \frac{\eta \cos(\alpha_\omega L) + 1 - \eta}{\cos(\alpha_\omega L) + \frac{1}{\xi_\omega} \frac{\sin(\alpha_\omega L)}{(\alpha_\omega L)}} \right|^2. \quad (22)$$

Figure 2 shows the frequency dependences of the plasmonic factor $|P_\omega|^2$ calculated for the GPIN-FETs with $L = 1.0 \mu\text{m}$, $w = 50 \text{ nm}$, $\mu = 100 \text{ meV}$, $\kappa = 4.5$, $\tau^i \simeq 0.1 \text{ ps}^{-1}$ ($c^i \simeq 0.5$), $\Omega/2\pi = 1.0 \text{ THz}$, and $\eta = 0.1$ at $\bar{\Phi} = 100 \text{ mV}$, i.e., $\bar{U} \simeq 200 \text{ mV}$ and $\gamma \simeq 2$ (see Table I).

As seen in Fig. 2, $|P_\omega|^2$ and, consequently, the rectified current components given by Eqs. (21), exhibit two pronounced maxima (in the frequency range under consideration, $\omega/2\pi \leq 4 \text{ THz}$).

The first maximum at $\omega/2\pi \simeq 1 \text{ THz}$ corresponds to the signal frequency close to the gated regions plasma frequency $\Omega/2\pi$. It is obviously related to the excitation (by the incoming signal) of the fundamental mode of standing plasma wave with the wavenumber $q_1 \simeq \pi/2L$ and the maximum amplitude at $x = \pm l$ having the opposite phases. As a result, $|\delta\Phi_\omega|$ and $|\delta J_\omega|$ are maximal. The collisional damping of this plasma oscillations results in lowering of the plasma resonance peaks [see the curves corresponding to different ν in Fig. 2(a)].

The second resonant peaks of $|P_\omega|^2$ at $\omega/2\pi \lesssim 3 \text{ THz}$ seen in Fig. 2 correspond to the excitation of the plasmonic mode with the wavenumber $q_3 \simeq 3\pi/2L$. It is instructive that the peaks associated with this mode can be higher than those related to the fundamental mode.

At elevated signal frequencies Eqs. (21) and (22) yield

$$\Delta\bar{J}_\omega \propto |P_\omega|^2 \propto \left(\frac{\bar{\omega}}{\omega}\right)^2, \quad (23)$$

where

$$\bar{\omega} = \frac{1}{\tau^i} \left(\frac{\pi\nu}{2\Omega} \right) \left(\frac{\sigma^g}{2\sigma^i} \right).$$

For the parameters of samples (a-1) - (a-3), one obtains $\bar{\omega}/2\pi \simeq 4.8 \text{ THz}$. The roll-off of $\Delta\bar{J}_\omega$ and $|P_\omega|^2$ with increasing frequency is determined by the charging time τ^i , i.e., is associated with the i-region geometrical capacitance c^i . Considering that $\sigma^g \propto 1/\nu$, one can find that $\bar{\omega}$ is independent of ν .

V. GPIN-FET DETECTOR RESPONSIVITY

The current responsivity (Ampere-Watt) of GPIN-FETs operating as the THz detectors is given by

$$R_\omega^J = \frac{\Delta\bar{J}_\omega H}{SI_\omega}, \quad (24)$$

where H is the lateral size of the GPIN-FET in the direction perpendicular to the gate edges, $S = \lambda_\omega^2 g/4\pi$ and $g \sim 1.5$ are the antenna aperture and gain, $\lambda_\omega = 2\pi c/\omega$ and I_ω are the wavelength and intensity of the incoming radiation, and c is the speed of light in vacuum. Considering that $\delta U_\omega^2 = 8\pi\lambda_\omega^2 I_\omega/c$, using Eq. (24), we obtain

$$R_\omega^J = \bar{R}^J |P_\omega|^2, \quad \bar{R}^J = \frac{4\pi^2 H \sigma^i \gamma}{cg \bar{U}}. \quad (25)$$

For the voltage (Volt-Watt) responsivity $R_\omega^V = r^{\text{load}} R_\omega^J$, assuming that the load resistance is optimized ($r^{\text{load}} = 3/2\sigma^i H$, i.e., $\gamma \simeq 2$ if $\sigma^i \ll \sigma^g/2$), we arrive at the following universal formula:

$$R_\omega^V = \bar{R}^V |P_\omega|^2, \quad \bar{R}^V = \frac{6\pi^2 \gamma}{cg \bar{U}}. \quad (26)$$

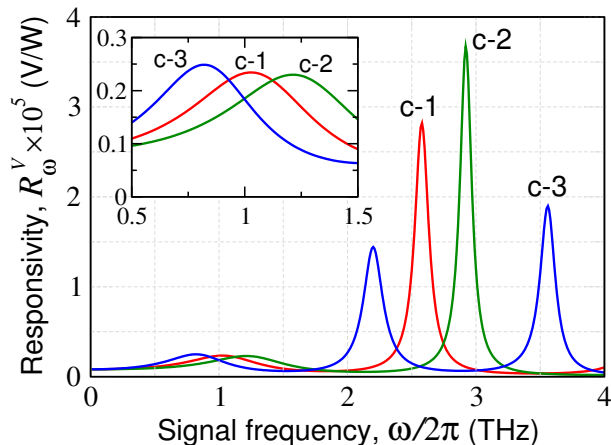


FIG. 3. Frequency dependences of Volt-Watt responsivity for the GPIN-FETs (c-1) - (c-3) - with different values of the carrier Fermi energy μ , conductance σ^g , and plasma frequency Ω ($\bar{U} = 200$ mV). Inset shows the vicinity of the fundamental resonance in more detail.

For $\bar{U} = (200 - 400)$ mV, we obtain $\bar{R}^V \simeq (1.12 - 0.56) \times 10^4$ V/W. If $2l = 0.2$ μm , $H = 10$ μm , and $\bar{U} = (200 - 400)$ mV, the optimized load resistance is equal to $r^{load} \simeq (307 - 216)$ Ω . Naturally, the plasmonic resonance may lead to $R_\omega^V \gg \bar{R}^V$.

A decrease in \bar{R}^V and, hence, in R_ω^V with the rise of the bias DC voltage \bar{U} is attributed to a decrease in the current-voltage characteristic nonlinearity parameter β [see Eq. (19)], and to a decrease in the channel resistance with rising bias voltage \bar{U} . The latter requires the pertinent decrease in the optimized load resistance r^{load} . However, lowering of the bias voltage is limited by the thermionic and thermogeneration processes in the i-region.

Figure 3 shows the GPIN-FET responsivity R_ω^V as a function of the signal frequency $\omega/2\pi$ calculated using Eqs. (25) and (26) involving Eq. (22) for the devices (c-1) - (c-3) with the parameters presented in Table I assuming $\bar{U} = 200$ mV.

First of all, one can see that GPIN-FETs can reveal fairly high peak responsivity. Second, the responsivity peaks corresponding to the higher plasma modes can be markedly higher than the fundamental peak (see the discussion in Sec. VI). Third, the second peaks (c-1) and (c-2) are positioned at the frequencies $\omega/2\pi$ somewhat lower than $\Omega/2\pi = 1.0$ THz and $\Omega/2\pi = 1.2$ THz, respectively. As was mentioned in Sec. IV, this is due to the effect of the i-region capacitance on the resonant frequency deviating it from the plasma frequency of the gated region Ω . The same is valid for the second and third peaks (c-3).

VI. DISCUSSION (ANALYSIS)

Temperature dependence and heights of the resonant peaks

The obtained formulas for the GPIN-FET responsivity R_ω^V do not explicitly account for the temperature dependence, at least at $\mu \gg T$, i.e., in the situations under consideration. This is because of the tunneling nature of the current in the GPIN-FETs. However, the plasmonic resonant factor, which determines the maximum values of R_ω^V is sensitive to the collision frequency ν . The latter is usually smaller at lower temperatures due to a decrease in the carrier momentum relaxation on acoustic phonons. Hence lowering of the temperature can result in a marked sharpening of the resonant responsivity peaks and promote a substantial increase in the resonant responsivity.

Figures 2 and 3, show some deviation of the resonant peaks position from the exact plasmonic resonances $\omega/2\pi = \Omega/2\pi = 1$ THz and $\omega/2\pi = 3$ THz - the peaks are shifted toward smaller frequencies. This is attributed to the collisional damping and to the contribution of the i-region geometrical capacitance. Indeed, as seen from Fig. 4, the GPIN-FETs with longer charging time τ^i , i.e., a larger i-region geometrical capacitance c^i due to a larger dielectric constant of the gate layer κ (and the same collisional frequency ν) exhibit smaller resonant frequencies. The gate layer in the samples (a-1) - (d-1) is assumed to be made of hBN ($\kappa = 4.5$), whereas the gate layers in the samples (d-2) and (d-3) are made of SiC ($\kappa = 10$) and HfO₂ ($\kappa = 15$), respectively. We also added the plot (see the dashed curve) corresponding to the parameters similar to those of the sample (d-1), but with a shorter charging time (smaller dielectric constant, $\kappa = 2.25$). As seen, the pertinent peak is shifted weaker than others. This confirms that the i-region geometrical capacitance markedly affects the plasmonic resonances.

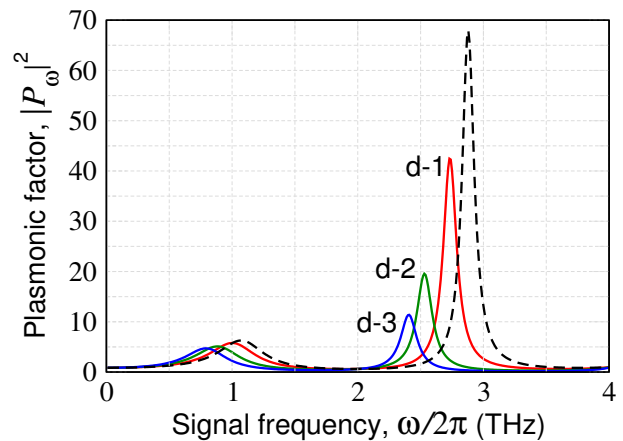


FIG. 4. Plasmonic factor $|P_\omega|^2$ versus signal frequency $f = \omega/2\pi$ for GPIN-FETs (d-1) - (d-3), which differ by charging time τ^i (proportional to gate layer dielectric constants κ). Dashed line corresponds to $\tau^i = 0.05$ ps ($\kappa = 2.25$).

The most intriguing feature of the $|P_\omega|^2$ and R_ω^V frequency dependences is the larger height of the peaks corresponding to a higher plasmonic mode. Compare the plasmonic factors at the fundamental and second resonance. The plasmonic factor $|P_\omega|^2$ near the fundamental ($\omega \simeq \Omega$) and the second ($\omega \simeq 3\Omega$) resonances (at $\eta \simeq 0$), $\nu \ll \Omega$, and $3\Omega\tau^i \ll 1$ is equal to

$$|P_\Omega|^2 \simeq \frac{(4\Omega/\pi\nu)^2}{\left|1 + \frac{8}{\pi} \left(\frac{2\sigma^i}{\sigma^g}\right) \mathcal{J}_0(\Omega t^i/2) e^{i\Omega t^i/2}\right|^2} \quad (27)$$

and

$$|P_{3\Omega}|^2 \simeq \frac{(12\Omega/\pi\nu)^2}{\left|1 - \frac{24}{\pi} \left(\frac{2\sigma^i}{\sigma^g}\right) \left(\frac{\Omega}{\nu}\right)^2 \mathcal{J}_0(3\Omega t^i/2) e^{i\Omega t^i/2}\right|^2} \quad (28)$$

respectively.

Considering that the product $\sigma^g\nu$ and, therefore, the denominators in the right-hand sides of Eqs. (27) and (28) are independent of ν , one can find that $|P_\Omega|^2 \propto (\Omega/\nu)^2$ and $|P_{3\Omega}|^2 \propto (\Omega/\nu)^2$. Such dependences of the plasmonic factor peaks on ν are in line with the plots in Fig. 1(a).

As follows from Eqs. (27) and (28), the ratio of the peak heights corresponding to the fundamental and the second resonance, at sufficiently large values $(2\sigma^i/\sigma^g)(\Omega/\nu)$, is equal to

$$n \simeq \left| \frac{P_{3\Omega}}{P_\Omega} \right|^2 \simeq \left[\frac{\mathcal{J}_0(\Omega t^i/2)}{\mathcal{J}_0(3\Omega t^i/2)} \right]^2. \quad (29)$$

This quantity can be smaller or larger than unity, depending on Ωt^i . For all the samples considered above [except (b-3)] $n > 1$, hence, the plasmonic resonances at $\omega \sim 3\Omega$ is stronger than those at $\omega \simeq \Omega$. This corresponds to the curves (a-1) -(b-2) in Fig. 2. In contrast, the case (b-3) is related to $n < 1$. In particular, for samples (a-1) and (b-1), we obtain $|P_\Omega|^2 \simeq 4.44$, $|P_{3\Omega}|^2 \simeq 42.37$, and $n \simeq 9.54$. This agrees well with the numerical calculations results shown in Fig. 2.

As mentioned above, the height of $|P_\omega|^2$ and R_ω^V resonant peaks decreases with increasing collision frequency ν . This is due to the strengthening of the plasma oscillation collisional damping. The hole and electron viscosity also damp the plasma oscillations, particularly, those with larger wavenumbers q . This might be a reason for some lowering of the resonant peaks corresponding to higher plasma oscillations modes. The effect of the viscosity can be accounted for by replacing ν by $\nu^{visc} = \nu + hq^2$ where h is the electron viscosity [1, 29, 41, 42]. For the fundamental, second, and the third plasma modes with $\omega_1 \simeq \Omega$, $\omega_2 \simeq 3\Omega$ and $\omega_3 \simeq 5\Omega$, the wavenumbers are $q_1 = \pi/2L$, $q_2 = 3\pi/2L$, and $q_3 = 5\pi/2L$. If $L = 1 \mu\text{m}$, setting $\nu = (1 - 2) \text{ps}^{-1}$

and $h = (100 - 500) \text{cm}^2/\text{s}$ (depending on the carrier density and the temperature [29, 41, 42]), $(\nu_1^{visc} - \nu)/\nu \simeq 0.0123 - 0.123$ and $(\nu_2^{visc} - \nu)/\nu \simeq 0.11 - 1.11$, these estimates show that the viscosity effect can decrease the heights of the second and fundamental peaks if the viscosity is sufficiently strong. As a result, the quantity $P_{3\Omega}$ [for example, for the samples (a-1) and (b-1)] can vary from $|P_{3\Omega}|^2 \simeq 42$ at $h = 0$ to $|P_{3\Omega}|^2 \simeq 34$ and 20 at $h = 100 \text{cm}^2/\text{s}$ and $h = 500 \text{cm}^2/\text{s}$, respectively. Lowering of the fundamental resonant peak is markedly smaller - about (2 -12) %. However, the second resonance remains stronger even at relatively high viscosity.

As for the third resonant peaks with $\omega_3 \simeq 5\Omega$ and $q_3 \simeq 5\pi/2L$, the plasma oscillation damping due to the viscosity is strong enough to lead to the peak extinction (the right most peak in Fig. 3) at $h = 500 \text{cm}^2/\text{s}$ and higher.

Effect of the contacts and gates coupling

As follows from Eq. (16), the plasmonic factor depends to some extent on the capacitive coupling between the side contacts and the gates. Figure 4 shows examples of the $|P_\omega|^2$ versus signal frequency $\omega/2\pi$ for the GPIN-FETs with the parameters corresponding to the sample (a-2) for $\eta = 0.1$ [as in Fig. 2(a)] and for $\eta = 0.2$ at $\bar{U} = 200 \text{mV}$. One can see that an increase in η leads to resonant peaks lowering. Although one needs to keep in mind that the value $\eta = 0.2$ corresponds to an overestimated contact-gate capacitance C_{cg} compared to typical values for FETs. For the comparison, we calculated $|P_\omega|^2$ also for a similar device structure, but with the short-cut side contacts and gates. In the latter case, one can use the following formula [coinciding with Eq. (22) with $\eta = 1$]:

$$|P_\omega|^2 = \frac{1}{\left|1 + \frac{1}{\xi_\omega} \frac{\tan(\alpha_\omega L)}{(\alpha_\omega L)}\right|^2}. \quad (30)$$

The pertinent dependence is shown in Fig. 5 as a dotted line. As seen in the latter case, the plasma resonance associated with the gated regions (at $\omega \sim \Omega$) is suppressed, while the plasmonic resonance at $\omega \sim 2\Omega$ is sufficiently pronounced although being relatively weak.

Thermionic and thermogeneration currents in the reverse-biased i-region

When $\bar{\Phi} \propto \bar{U}$ becomes relatively low, the reverse thermionic current in the reverse-biased i-region can be comparable with the tunneling current. Considering the tunneling current [given by Eq. (1)] and the saturation current [given by Eq. (C2)], we find the following limitation for the minimal value of \bar{U} at which the tunneling dominates over the thermionic processes:

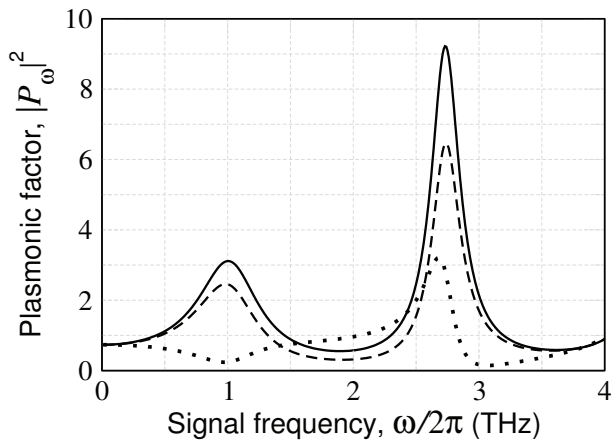


FIG. 5. Plasmonic factor $|P_\omega|^2$ versus signal frequency $f = \omega/2\pi$ for the sample with the same parameters as the sample (a-2) and $\eta = 0.1$ (solid line) and $\eta = 0.2$ (dashed line). The dotted line is related to a GPIN-FET with the parameters (a-2), but short-cut side contacts and the pertinent gates.

$$e\bar{\Phi} > \left(\frac{6}{b\pi^2}\right)^{2/3} \left(\frac{2l\mu^2 T^2}{\hbar v_W}\right)^{1/3} \exp\left(-\frac{2\mu}{3T}\right) = e\bar{\Phi}_{min} \quad (31)$$

For $2l = 0.2 \mu\text{m}$, $\mu = 100 \text{ meV}$, and $T = 25 \text{ meV}$, one obtains $e\bar{\Phi}_{min} \simeq 17.5 \text{ meV}$. This condition was satisfied in the above estimates and calculations.

The thermogeneration of the electron-hole pairs in the reverse-biased graphene p-i-n junction is primarily associated with the interband absorption of optical phonons. The thermionic rate at room temperature is estimated as $g^{therm} = 10^{21} \text{ cm}^{-2}\text{s}^{-1}$ [43]. For $2l = 0.2 \mu\text{m}$, the latter yields $J^{therm} = 4elg^{therm} \simeq 6.4 \times 10^{-3} \text{ A/cm}$. For comparison, the tunneling current density in the reverse-biased p-i-n junction given by Eq. (1) for the same lengths of the i-region at $e\bar{\Phi} = (100 - 200) \text{ meV}$, is equal to $\bar{J}^i \simeq (0.34 - 0.95) \text{ A/cm}$, i.e., one order of magnitude larger. This implies that the dark current in the GPIN-FETs in the conditions under consideration is determined by the interband tunneling in the i-regions.

Joule heating

The Joule power in the GPIN-FET is equal to $Q = H\bar{J}\bar{V}$. For $\bar{\Phi} \lesssim \bar{V} = 100 - 200 \text{ mV}$ ($\bar{U} \simeq 200 - 400 \text{ mV}$), $\bar{J} \lesssim (0.5 - 1.0) \text{ A/cm}$. Assuming the device width $H = 10 \mu\text{m}$, for the Joule power we obtain $Q \simeq (5 - 10) \times 10^{-5} \text{ W}$. Since the bias voltage drops primarily in the i-region and somewhat around it, the Joule power releases in the area of about $2lH$. This corresponds to the thermal power density $Q/2lH$. For $2JH = 2 \times 10^{-8} \text{ cm}^2$, we obtain $Q/2lH \simeq (2.5 - 5.0) \text{ kW/cm}^2$. The latter thermal power density is much lower than that, which can be supported by GFETs (up to 210 kW/cm^2 [44, 45]). Hence, the Joule heating should not lead to a marked

overheating of the GPIN-FET channel. Indeed, the heat flow from the GPIN-FET channel through, for example, the hBN substrate can be estimated considering the hBN thermal conductivity $k_{th} \simeq 20 \text{ W/m}\cdot\text{K}$ [46]. Assuming the thickness of the hBN layer $D = (1 - 2) \mu\text{m}$, we for the thermal conductivity per unit area $K_{th} = k_{th}/D \simeq (1 - 2) \text{ kW/cm}^2\text{K}$. This implies that, in such a case, the Joule heating results in an increase of the channel temperature by $\Delta T \lesssim 5 \text{ K}$. Since graphene has a high room-temperature thermal conductivity (about $k_{th} = 5 \text{ kW/m}\cdot\text{K}$) [47], the heat can also be effectively carried to the side (metallic) contacts.

Comparison of the Zener-Klein tunneling nonlinearity mechanisms with some other mechanisms

It appears natural to compare the mechanisms of the current rectification in the GPIN-FETs under consideration and in similar detectors (for example, [8]). In the latter devices, the $I - V$ characteristic nonlinearity in the forward-biased graphene p-n junction is used. The pertinent nonlinearity parameter β^{th} is given by Eq. (C3). Comparing the quantities β [see Eq. (19)] and β^{th} (for $\bar{\Phi} = -\bar{\Phi}^{th} < 0$ in the case of the detector using the p-n nonlinearity) and $\bar{\Phi} > 0$ for the GPIN-FET, we obtain

$$\frac{\beta}{\beta^{th}} \simeq \frac{\pi^2 b}{8} \sqrt{\frac{\hbar v_W}{2l}} \frac{T \exp[(\mu - e\bar{\Phi}^{th})/T]}{\mu \sqrt{e\bar{\Phi}}} \quad (32)$$

Setting $2l = 0.2 \mu\text{m}$, $\mu = 100 \text{ meV}$, $\bar{\Phi} = 100 \text{ mV}$, $\bar{\Phi}^{th} = 25 \text{ mV}$, we obtain at $T = 25 \text{ meV}$ ($\simeq 300 \text{ K}$) and $\beta/\beta^{th} \simeq 0.1$. At the temperatures below room temperature, this ratio can be markedly larger. For example, at $T = (7.5 - 10) \text{ meV}$ [$\simeq (90 - 120) \text{ K}$], one obtains $\beta/\beta^{th} \simeq 1 - 9$.

VII. CONCLUSIONS

We demonstrated that the proposed GPIN-FETs detectors using the signal rectification due to the nonlinearity of the Zener-Klein tunneling $I - V$ characteristics can exhibit high responsivity in the THz range of frequencies. The responsivity can be particularly high at the signal frequencies close to the fundamental and triple carrier plasma frequency. This is due to the resonant excitation of plasma oscillation in the gate region of the GPIN-FET channel. The GPIN-FETs can demonstrate competitive resonant responsivity at room temperatures. At lower temperatures, the responsivity can markedly increase due to the reinforcement of the resonant response because of a weakening of the carrier momentum relaxation.

ACKNOWLEDGMENTS

The Japan Society for Promotion of Science (KAKENHI Grants # 21H04546 and # 20K20349), Japan; RIEC Nation-Wide Collaborative Research Project # R04/A10; the US Office of Scientific Research Contract N00001435, (Project Monitor Dr. Ken Goretta).

DISCLOSURE

The authors declare no conflict of interest related to this article.

APPENDIX A

Dynamic tunneling conductance of the reverse-biased i-region

The injected holes and electrons propagating in the i-region induce the current in the surrounding highly conducting (gated) regions. The dynamical conductance, apart from the DC differential conductance σ^i of the reverse-biased i-region found from Eq. (1), should account for the displacement current associated with the geometrical capacitance c^i . Therefore, the dynamical conductance of the i-region associated with the propagating carriers can be presented as

$$\sigma_\omega^i = \sigma^i F_\omega - i\omega c^i. \quad (\text{A1})$$

Due to a strong nonuniformity of the electric field in the i-region, the tunneling generation of the electrons and holes occurs near the edges of the p- and n-regions, respectively. If the generated holes and electrons propagate across the i-region ballistically, their velocities are equal to $\pm v_W$. Therefore, the AC electron and hole currents are proportional to $\exp(i\omega x/v_W)$ and $\exp(-i\omega x/v_W)$. Hence, the AC current induced by the propagating carriers is proportional to

$$F_\omega = \frac{1}{2l} \int_{-l}^l dx g(x) [\exp(i\omega x/v_W) + \exp(-i\omega x/v_W)],$$

where, for the case of the device geometry under consideration (blade-like conducting areas), the form-factor $g(x)$ is given by $g(x) = 2/\pi\sqrt{1 - (x/l)^2}$ [48]. This leads to

$$F_\omega = \frac{2}{\pi} e^{i\omega t^i/2} \int_0^1 ds \frac{\cos(\omega t^i s/2)}{\sqrt{1-s^2}} = e^{i\omega t^i/2} \mathcal{J}_0(\omega t^i/2), \quad (\text{A2})$$

where $t^i = 2l/v_W$ and $\mathcal{J}_0(s)$ is the Bessel function of the first kind.

If the potential drop, $\overline{\Phi} > \hbar\omega_0$, the optical phonon emission can delay the holes and electrons propagation in the i-region. For $\overline{\Phi}$ markedly exceeding 200 mV, the spatial dependence of the carrier velocity can be presented as $v_x = \pm v_W \exp(-x/\tau_{op}v_W)$, where $\tau_{op} \simeq (1-2)$ ps [43] is the time of the optical phonon spontaneous emission. For the average transit time $\langle t^i \rangle = (1/2l) \int_{-l}^l dx (2l/v_x)$, we obtain $\langle t^i \rangle = 2\tau_{op} \sinh(t^i/v_W\tau_{op}) \simeq t^i(1 + t^i/12\tau_{op}) \gtrsim t^i$. For $2l = (0.2 - 0.5) \mu\text{m}$, the latter estimate yields $\langle t^i \rangle / t^i - 1 \gtrsim (1 - 4)\%$.

The i-region capacitance c^i , which determines the capacitive component of the displacement current through the i-region, for the blade-like conducting areas can be estimated, generalizing [33, 49] by accounting for the presence of the highly conducting gates, as

$$c^i = \frac{\kappa}{2\pi^2} \Lambda, \quad \text{or} \quad c^i = \frac{\kappa^{eff}}{2\pi^2} \Lambda, \quad (\text{A3})$$

where Λ , as in [33, 49], is a logarithmic factor, which weakly depends on the geometrical parameters. Equation (A3) for the GPIN-FET with $\kappa = 4.5$, yields $c^i \gtrsim 0.5$. This value is used in the main text.

APPENDIX B

In the gradual channel approximation, the spatio-temporal distributions of the electron and hole densities, $\Sigma^n(x, t)$ and $\Sigma^p(x, t)$, in the gated regions are related to the channel potential, $\varphi(x, t)$, and the gate potentials, $\varphi_g^n(t)$ and $\varphi_g^p(t)$, as

$$\Sigma^n(x, t) = \frac{\kappa}{4\pi ew} [\varphi_g^n(t) - \varphi(x, t)], \quad (\text{B1})$$

$$\Sigma^p(x, t) = \frac{\kappa}{4\pi ew} [\varphi_g^p(t) + \varphi(x, t)], \quad (\text{B2})$$

where κ and w are the gate layer dielectric constant and thickness. If the side source/drain contacts and the gates are coupled by a capacitive link associated with a free-space parasitic contact-gate capacitance [see Fig. 1(a)],

$$\varphi_g^n(t) = V_g + \frac{C_{cg}}{C_g + C_{cg}} \frac{U(t)}{2}, \quad (\text{B3})$$

$$\varphi_g^p(t) = -V_g - \frac{C_{cg}}{C_g + C_{cg}} \frac{U(t)}{2}, \quad (\text{B4})$$

where C_{cg} and C_g are the contact-gate and gate-channel capacitances, respectively.

For the DC electron and hole densities, from Eqs. (B1) and (B2) one obtains

$$\begin{aligned}\bar{\Sigma}^n &= \frac{\kappa}{4\pi e} \left[V_g + \frac{\eta}{2} \bar{U} - \bar{\varphi}(x) \right] \\ &\simeq \frac{\kappa}{4\pi e} \left(V_g + \frac{\eta}{2} \bar{U} \right) = \bar{\Sigma},\end{aligned}\quad (\text{B5})$$

$$\begin{aligned}\bar{\Sigma}^p &= \frac{\kappa}{4\pi e} \left[V_g + \frac{\eta}{2} \bar{U} + \bar{\varphi}(x) \right] \\ &\simeq \frac{\kappa}{4\pi e} \left(V_g + \frac{\eta}{2} \bar{U} \right) \bar{\Sigma}\end{aligned}\quad (\text{B6})$$

with $\eta = C_{cg}/(C_g + C_{cg})$. Since normally the DC bias voltage $\bar{V} < \bar{U} \ll V_g$, in Eqs. (B5) and (B6) we omitted the spatially nonuniform terms with $\bar{\varphi}(x)$.

For the Fourier AC components, Eqs. (B1) - (B4) yield

$$\delta\Sigma_\omega^n(x) = \frac{\kappa}{4\pi e w} \left[\frac{\eta}{2} \delta V_\omega - \delta\varphi_\omega(x) \right], \quad (\text{B7})$$

$$\delta\Sigma_\omega^p(x) = \frac{\kappa}{4\pi e w} \left[-\frac{\eta}{2} \delta V_\omega + \delta\varphi_\omega(x) \right]. \quad (\text{B8})$$

Since the load resistance is shunt by a large capacitance and the drop of the AC potential across the load resistor is insignificant, $\delta U_\omega = \delta V_\omega$.

As usually, considering the linearized hydrodynamic equations, expressing the electron and hole average velocities, δu_ω^n and δu_ω^p , via the AC electric field $-d\delta\varphi_\omega(x)/dx$, and substituting δu_ω^n and δu_ω^p into the continuity equation, we obtain

$$\frac{d^2\delta\varphi_\omega}{dx^2} - \frac{m\omega(\omega + i\nu)}{e\bar{\Sigma}} \delta\Sigma^n = 0, \quad (\text{B9})$$

$$\frac{d^2\delta\varphi_\omega}{dx^2} - \frac{m\omega(\omega + i\nu)}{e\bar{\Sigma}} \delta\Sigma^p = 0, \quad (\text{B10})$$

where m is the fictitious electron/hole mass in graphene. Expressing m and $\bar{\Sigma}$ via the carrier Fermi energy, μ , in the gated region, we arrive at Eq. (9) in the main text.

If the side contacts and the gates are shortened, one can again obtain Eq. (16), but with $\eta = 1$.

APPENDIX C

The thermionic DC current density, including both the hole and electron components, in the i-region of the GPIN-FETs under consideration can be presented as

$$\bar{J}^{th} = J_s \exp\left(-\frac{\mu}{T}\right) \left[\exp\left(-\frac{e\bar{\Phi}^{th}}{T}\right) - 1 \right], \quad (\text{C1})$$

where

$$J_s \simeq \frac{4eT\mu}{\pi^2\hbar^2 v_W} \exp\left(-\frac{\mu}{T}\right) \quad (\text{C2})$$

is the saturation current density of GL p-i-n junctions. In Eq. (C1), as in the main text, the p-i-n junction reverse and forward bias voltages $\bar{\Phi} > 0$ and $\bar{\Phi}^{th} < 0$, respectively.

Equations (C1) and (C2) yield the following value of the $I - V$ characteristic nonlinearity parameter:

$$\begin{aligned}\beta^{therm} &= \frac{1}{2} \frac{d^2\bar{J}^{therm}}{d\bar{\Phi}^2} = \frac{\sigma^{i,th}}{2T} \\ &\simeq \frac{2e^3}{\pi^2\hbar^2 v_W} \left(\frac{\mu}{T}\right) \exp\left(-\frac{\mu + e\bar{\Phi}}{T}\right)\end{aligned}\quad (\text{C3})$$

and $\sigma^{i,th}$ is the differential conductance.

-
- [1] M. I. Dyakonov and M. S. Shur, "Plasma wave electronics: novel terahertz devices using two-dimensional electron fluid," *IEEE Trans. Electron. Devices* **43**, 1640(1996).
- [2] A. Zak, M. A. Andersson, M. Bauer, J. Matukas, A. Lisauskas, H. G. Roskos, and J. Stake, "Antenna-integrated 0.6 THz FET direct detectors based on CVD graphene," *Nano Lett.* **14**, 5834 (2014).
- [3] L. Vicarelli, M. S. Vitiello, D. Coquillat, A. Lombardo, A. C. Ferrari, W. Knap, M. Polini, V. Pellegrini, and A. Tredicucci, "Graphene field-effect transistors as room temperature terahertz detectors," *Nat. Mat.* **11**, 865 (2012).
- [4] F. H. L. Koppens, T. Mueller, P. Avouris, A. C. Ferrari, M. S. Vitiello, and M. Polini, "Photodetectors based on graphene, other two-dimensional materials and hybrid systems," *Nat. Nanotechnol.* **9**, 780 (2014).
- [5] V. V. Popov, N. Pala, and M. S. Shur, "Room temperature terahertz plasmonic detection by antenna arrays of field-effect transistors," *Nanosci. Nanotechnol. Lett.* **4**, 1015 (2012).
- [6] T. Otsuji, T. Watanabe, S. A. Boubanga Tombet, A. Satou, W. M. Knap, V. V. Popov, M. Ryzhii, and V. Ryzhii, "Emission and detection of terahertz radiation using two-dimensional electrons in III-V semiconductors and graphene," *IEEE Trans. Terahertz Sci. Technol.* **3**, 63 (2013).
- [7] T. Otsuji, T. Watanabe, S. A. Boubanga Tombet, A.

- Satou, V. Ryzhii, V. Popov, and W. Knap, "Emission and detection of terahertz radiation using two-dimensional plasmons in semiconductor nanoheterostructures for nondestructive evaluations," *Opt. Eng.* **53**, 031206 (2014).
- [8] V. Ryzhii, M. Ryzhii, M. S. Shur, V. Mitin, A. Satou, and T. Otsuji, "Resonant plasmonic terahertz detection in graphene split-gate field-effect transistors with lateral p-n junctions," *J. Phys. D: Appl. Phys.* **49**, 315103 (2016).
- [9] D. Yadav, S. Boubanga-Tombet, T. Watanabe, S. Arnold, V. Ryzhii, and T. Otsuji, "Terahertz wave generation and detection in double-graphene layered van der Waals heterostructures," *2D Mater.* **3**, 045009 (2016).
- [10] D. V. Fateev, K. V. Mashinsky, and V. V. Popov, "Terahertz plasmonic rectification in a spatially periodic graphene," *Appl. Phys. Lett.* **110**, 0611106 (2017).
- [11] I. A. Gayduchenko, G. E. Fedorov, M. V. Moskotin, D. I. Yagodkin, S. V. Seliverstov, G. N. Goltsman, A. Yu. Kuntsevich, M. G. Rybin, E. D. Obratsova, V. G. Leiman, M. S. Shur, T. Otsuji, and V. I. Ryzhii, "Manifestation of plasmonic response in the detection of sub-terahertz radiation by graphene based devices," *Nanotechnology* **29**, 245204 (2018).
- [12] D. A. Bandurin, D. Svintsov, I. Gayduchenko, S. G. Xu, A. Principi, M. Moskotin, I. Tretyakov, D. Yagodkin, S. Zhukov, T. Taniguchi, K. Watanabe, I. V. Grigorieva, M. Polini, G. N. Goltsman, A. K. Geim, and G. Fedorov, "Resonant terahertz detection using graphene plasmons," *Nat. Comm.* **9**, 5392 (2018).
- [13] V. Ryzhii, T. Otsuji, and M. S. Shur, "Graphene based plasma-wave devices for terahertz applications," *Appl. Phys. Lett.* **116**, 140501 (2019).
- [14] V. V. Cheianov and V. I. Fal'ko, "Selective transmission of Dirac electrons and ballistic magnetoresistance of n-p junctions in graphene," *Phys. Rev.* **74**, 041103 (2006).
- [15] A. Ossipov, M. Titov, and C. W. J. Beenakker, "Reentrance effect in a graphene n-p-n junction coupled to a superconductor," *Phys. Rev. B* **75**, 241401(R) (2007).
- [16] D. Jena, "Tunneling transistors based on graphene and 2-D crystals," *Proc. IEEE* **101**, 1585 (2013).
- [17] N. Vandecasteele, A. Barreiro, M. Lazzeri, A. Bachtold, and F. Mauri, "Current-voltage characteristics of graphene devices: Interplay between Zener-Klein tunneling and defects," *Phys. Rev. B* **82**, 045416 (2010).
- [18] V. Ryzhii, M. Ryzhii, V. Mitin, and M. S. Shur, "Graphene tunneling transit-time terahertz oscillator based on electrically induced p-i-n junction," *Appl. Phys. Exp.* **2**, 034503 (2009).
- [19] V. L. Semenenko, V. G. Leiman, A. V. Arsenin, V. Mitin, M. Ryzhii, T. Otsuji, and V. Ryzhii, "Effect of self-consistent electric field on characteristics of graphene p-i-n tunneling transit-time diodes," *J. Appl. Phys.* **113**, 024503 (2013).
- [20] J. C. Song, D. A. Abanin, and L. S. Levitov, "Coulomb drag mechanisms in graphene," *Nano Lett.* **13**, 3631 (2013).
- [21] M. Schütt, P. M. Ostrovsky, M. Titov, I. V. Gornyi, B. N. Narozhny, and A. D. Mirlin, "Coulomb drag in graphene near the Dirac point," *Phys. Rev. Lett.* **110**, 026601 (2013).
- [22] R. V. Gorbachev, A. K. Geim, M. I. Katsnelson, K. S. Novoselov, T. Tudorovskiy, I. V. Grigorieva, A. H. MacDonald, S. V. Morozov, K. Watanabe, T. Taniguchi, and L. A. Ponomarenko, "Strong Coulomb drag and broken symmetry in double-layer graphene," *Nat. Phys.* **8**, 896 (2012).
- [23] V. Ryzhii, M. Ryzhii, V. Mitin, M. S. Shur, and T. Otsuji, "S-shaped current-voltage characteristics of n+-i-n+ graphene field-effect transistors due the Coulomb drag of quasi-equilibrium electrons by ballistic electrons," *Phys. Rev. Appl.* **16**, 014001 (2021).
- [24] V. Ryzhii, M. Ryzhii, A. Satou, T. Otsuji, V. Mitin, M. S. Shur, "Effect of Coulomb carrier drag and terahertz plasma instability in p+-p-i-n-n+ graphene tunneling transistor structures," *Phys. Rev. Appl.* **16**, 064054 (2021).
- [25] V. Ryzhii, M. Ryzhii, V. Mitin, M. S. Shur, and T. Otsuji, "Coulomb electron drag mechanism of terahertz plasma instability in n+-i-n-n+ graphene FETs with ballistic injection," *Appl. Phys. Lett.* **119**, 093501 (2019).
- [26] M. S. Shur and L. F. Eastman, "Ballistic transport in semiconductor at low temperatures for low-power high-speed logic," *IEEE Trans. Electron Devices* **26**, 1677 (1979).
- [27] A. Rahman, J. Guo, S. Datta, and M. S. Lundstrom, "Theory of ballistic nanotransistors," *IEEE Trans. Electron Devices* **50**, 1853 (2003).
- [28] G. Liang, N. Neophytou, D. E. Nikonov, and M. S. Lundstrom, "Performance projections for ballistic graphene nanoribbon field-effect transistors," *IEEE Trans. Electron Devices* **54**, 677 (2007).
- [29] Y. Zhang and M. S. Shur, "Collision dominated, ballistic, and viscous regimes of terahertz plasmonic detection by graphene," *J. Appl. Phys.* **129**, 053102 (2021).
- [30] X. Li, E. A. Barry, J. M. Zavada, M. Buongiorno Nardelli, and K. W. Kim, "Influence of electron-electron scattering on transport characteristics in monolayer graphene," *Appl. Phys. Lett.* **97**, 082101 (2010).
- [31] A. S. Mayorov, R. V. Gorbachev, S. V. Morozov, L. Britnell, R. Jalil, L. A. Ponomarenko, P. Blake, K. S. Novoselov, K. Watanabe, T. Taniguchi, and A. K. Geim, "Micrometer-scale ballistic transport in encapsulated graphene at room temperature," *Nano Lett.* **11**, 2396 (2011).
- [32] L. Banszerus, M. Schmitz, S. Engels, M. Goldsche, K. Watanabe, T. Taniguchi, B. Beschoten, and C. Stampfer, "Ballistic transport exceeding 28 μm in CVD grown graphene," *Nano Lett.* **16**, 1387 (2016).
- [33] S. G. Petrosyan and A. Ya. Shik, "Contact phenomena in low-dimensional electron systems," *Sov. Phys. -JETP* **69**, 2119 (1989).
- [34] B. L. Gelmont, M. S. Shur, and C. Moglestue, "Theory of junction between two-dimensional electron gas and p-type semiconductor," *IEEE Trans. Electron Devices* **39**, 1216 (1992).
- [35] D. B. Chklovskii, B. I. Chklovskii, and L. I. Glasman, "Electrostatics of edge channels," *Phys. Rev. B* **1992**, 46, 4026.
- [36] V. Ryzhii, A. Satou, I. Khmyrova, M. Ryzhii, T. Otsuji, V. Mitin, and M. S. Shur, "Plasma effects in lateral Schottky junction tunneling transit-time terahertz oscillator," *J. Phys. Conf. Ser.* **38**, 228 (2006).
- [37] V. Ryzhii, "Terahertz plasma waves in gated graphene heterostructures," *Jpn. J. Appl. Phys.* **45**, L923 (2006).
- [38] L. A. Falkovsky and A. A. Varlamov, "Space-time dispersion of graphene conductivity," *European Phys. J. B* **56**, 281 (2007).
- [39] V. Ryzhii, A. Satou, and T. Otsuji, "Plasma

- waves in two-dimensional electron-hole system in gated graphene,” *J. Appl. Phys.* **101**, 024509 (2007).
- [40] A. Soltani, F. Kuschewski, M. Bonmann, et al., “Direct nanoscopic observation of plasma waves in the channel of a graphene field-effect transistor,” *Light Sci. Appl.* **9**, 1 (2020).
- [41] A. I. Berdyugin, S. G. Xu, F. M. D. Pellegrino, R. K. Kumar, A. Principi, I. Torre, M. B. Shalom, T. Taniguchi, K. Watanabe, I. V. Grigorieva, M. Polini, A. K. Geim, and D. A. Bandurin, “Hall viscosity of graphene’s electron fluid,” *Science* **364**, 162 (2019).
- [42] A. Principi, G. Vignale, M. Carrega, and M. Polini, “Bulk and shear viscosities of the two-dimensional electron liquid in a doped graphene sheet,” *Phys. Rev. B* **93**, 125410 (2016).
- [43] F. Rana, P. A. George, J. H. Strait, S. Shivaraman, M. Chandrashekar, and M. G. Spencer, “Carrier recombination and generation rates for intravalley and intervalley phonon scattering in graphene,” *Phys. Rev. B* **79**, 115447 (2009).
- [44] M. Freitag, H.-Y. Chiu, M. Steiner, V. Perebeinos, and P. Avouris “Thermal infrared emission from biased graphene,” *Nat. Nanotechnol.* **5**, 497 (2008).
- [45] M. Freitag, M. Steiner, Y. Martin, V. Perebeinos, Z. Chen, J. C. Tsang, and P. Avouris, “Energy dissipation in graphene field-effect transistors,” *Nano Lett.* **9**, 1883 (2009).
- [46] J.-C. Zheng, L. Zhang, A. V. Kretinin, S. V. Morozov, Yi BoWang, T.Wang, X. Li, F. Ren, J. Zhang, C.-Yu Lu, J.-C. Chen, M. Lu, H.-Q. Wang, A. K. Geim, and K. Novoselov, “High thermal conductivity of hexagonal boron nitride laminates,” *2D Mat.* **3**, 011004 (2016).
- [47] A. A. Balandin, S. Ghosh, W. Bao, I. Calizo, D. Teweldebrhan, F. Miao, and C. Ning Lau, “Superior thermal conductivity of single-layer graphene,” *Nano Lett.* **8**, 902 (2008).
- [48] V. Ryzhii and G. Khrenov, “High-frequency operation of lateral hot-electron transistor,” *IEEE Trans. Electron Devices* **42**, 166 (1995).
- [49] A. Sh. Achoyan, A. É. Yesayan, É. M. Kazaryan, and S. G. Petrosyan, “Two-dimensional p-n junction under equilibrium conditions,” *Semiconductors*, **36**, 903 (2002).